Acta Materialia 230 (2022) 117847

Contents lists available at ScienceDirect

Acta Materialia

journal homepage: www.elsevier.com/locate/actamat

Full length article

Designing structures with combined gradients of grain size and precipitation in high entropy alloys for simultaneous improvement of strength and ductility

Shuang Qin[a], Muxin Yang[a], Ping Jiang[a], Jian Wang[a,b], Xiaolei Wu[a,b], Hao Zhou[c], Fuping Yuan[a,b,*]

[a] State Key Laboratory of Nonlinear Mechanics, Institute of Mechanics, Chinese Academy of Science, 15 Beisihuan West Road, Beijing 100190, China
[b] School of Engineering Science, University of Chinese Academy of Sciences, 19A Yuquan road, Beijing 100049, China
[c] Nano and Heterogeneous Materials Center, School of Materials Science and Engineering, Nanjing University of Science and Technology, Nanjing, China

ARTICLE INFO

Article history:
Received 12 January 2022
Revised 6 March 2022
Accepted 14 March 2022
Available online 16 March 2022

Keywords:
High-entropy alloys
Gradient structures
Precipitates
Strain hardening
Strengthening
Ductility

ABSTRACT

Suppressing the early strain localization at the nanostructured topmost layer is crucial for achieving better tensile ductility in the gradient structure. Thus, structures with combined gradient distributions along the depth for both grain size and volume fraction of precipitates were designed and introduced in a high entropy alloy by surface mechanical attrition treatment and aging. Yield strength and uniform elongation were observed to be simultaneously improved in the structures with combined gradients as compared to the corresponding structures with only grain size gradient. More severe strain gradients and higher density of geometrically necessary dislocations were observed to be produced at various domain boundaries in the structures with combined gradients, resulting in stronger hetero-deformation-induced (HDI) extra hardening for better tensile properties. Shearing and bowing hardening mechanisms were observed for $L1_2$ and B2 precipitates, respectively. Higher volume fractions of B2 and $L1_2$ phases at the topmost layer induce stronger precipitation hardening, which compensates the diminished strain hardening due to the reduced grain size at the topmost layer for better tensile ductility in the structures with combined gradients. The observed higher yield strength in the structures with combined gradients have been discussed based on mechanisms of dislocation strengthening, precipitation strengthening and HDI strengthening.

1. Introduction

High-entropy alloys (HEAs) [1–8] and medium-entropy alloys (MEAs) [9–16], defined as alloys consisting of multiple principal elements with equal or nearly equal molar fraction, have drawn extensive attentions due to their extraordinary tensile properties. For example, FCC single phase HEAs [1–3] and MEAs [9–13,17] generally show high ductility and fracture toughness at room temperature, and even better tensile properties and damage tolerance at cryogenic temperature, which can be attributed to a transition of the dominant deformation mechanism from dislocation slip to deformation twins. More interestingly, some unusual deformation mechanisms have been found in HEAs and MEAs due to the atomic inhomogeneity with chemical short-range order (CSRO) [18–23] and the spatially varied stacking fault energy (SFE) at nanoscale [15]. These unusual deformation mechanisms have been identified to be the changing dislocations slip modes, the enhanced friction resistance for dislocation slip and the accumulation of dislocations around the CSROs. While, the relative low yield strength for FCC HEAs and MEAs with coarse grains (CG) can restrict their structural applications. Cold working or grain refinement through severe plastic deformation can significantly increase the yield strength for metals and alloys, while such enhanced yield strength in homogeneous structures is generally accompanied with loss of ductility [24,25] and the long-lasting strength-ductility paradox for conventional alloys still exists for most HEAs and MEAs.

Recently, it has been reported that superior synergy of strength and ductility can be achieved and the strength-ductility trade-off can be resolved by gradient structures, in which the grain sizes, twin fraction, phase fraction or texture are gradually changed from the surface to the center [26–30]. Geometrically necessary dislocations (GNDs) can be induced in gradient structures during uniaxial tensile loading due to the strain gradients among different layers and the stress-state change for each layer, which thus results in

* Corresponding author at: State Key Laboratory of Nonlinear Mechanics, Institute of Mechanics, Chinese Academy of Science, 15 Beisihuan West Road, Beijing 100190, China.
E-mail address: fpyuan@lnm.imech.ac.cn (F. Yuan).

https://doi.org/10.1016/j.actamat.2022.117847
1359-6454/

extra strengthening and strain hardening [28,31]. Strain partitioning and stress transfer between various layers at different depths can also be induced due to the dramatically different mechanical properties for layers at varying depths, which can produce hetero-deformation-induced (HDI) hardening for better tensile properties [32,33].

Precipitation strengthen/hardening can also be considered as one efficient strategy for obtaining excellent tensile properties and for resolving the strength-ductility trade-off in metals and alloys [34–37], especially when the precipitates are at nanoscale and coherent with the matrix. Such strategy has been utilized to HEAs and MEAs with intermetallic particles, such as the ordered B2 and $L1_2$ particles, and the size, shape, volume fraction, type and distribution of precipitates have been carefully controlled and tailored to obtain excellent synergy of strength and ductility in such HEAs and MEAs [38–46]. Coherent nanoprecipitates are beneficial for mechanical properties, which can be attributed to the enhanced strength by blocking dislocations, and the improved strain hardening by the minimal lattice misfit at phase interfaces and by accumulating dislocations around coherent nanoprecipitates.

In general, the nanostructured topmost layer in the gradient structure has higher propensity for plastic instability, thus certain mechanism is needed for maintaining uniform deformation at topmost layer. For example, the grain boundary (GB) migration with concomitant grain coarsening at the topmost layer upon tensile loading provides significant contribution to uniform elongation for the pure copper with gradient structure, while such structural coarsening should sacrifice the strength and mechanical/thermal stability in some extent [29]. Enlighted by the benefits of gradient grain structures and nanoprecipitates, superior tensile properties could be achieved by deploying heterogeneous structures with combined gradients in HEAs and MEAs, in which both gradients from grain size (including substructures, such as dislocation cells) and volume fraction of nanoprecipitates exist. It is possible that the designed higher volume fractions of nanoprecipitates could provide stronger precipitation hardening at the topmost layer, which compensates the diminished strain hardening due to the reduced grain size at the topmost layer and prevents the early plastic deformation localization at the topmost layer, resulting in better tensile ductility in the structures with combined gradients. While such microstructures are rarely deployed in HEAs and MEAs, and the corresponding strain hardening/strengthening mechanisms for HEAs and MEAs with such structures with combined gradients have not been explored yet. Thus, we propose and design a structure with combined gradients in a non-equiatomic HEA ($Al_{0.5}Cr_{0.9}FeNi_{2.5}V_{0.2}$) with a high Ni concentration of $\sim$ 50% and a high Ni/Al ratio of $\sim$ 5, and the structures with combined gradients have been fabricated by surface mechanical attrition treatment (SMAT) followed by different heat treatments (annealing and aging). Moreover, the effects of the combined gradients on the mechanical properties and the corresponding deformation mechanisms have been revealed.

2. Materials and experimental techniques

The $Al_{0.5}Cr_{0.9}FeNi_{2.5}V_{0.2}$ (in atomic ratio) HEA was obtained by arc-melting under argon atmosphere, and were re-melted multiple times to insure chemical homogeneity. Then the ingots were hot-forged at 1100 °C followed by annealing at 1200 °C for 24 h and water quenching. The samples after annealing are referred to as-annealed samples here. The annealing plates were then processed by SMAT. The disks for SMAT were cut from the annealed plates by wire saw into dimensions of 70 × 60 × 1.1 mm^3. Both sides of the sample plates were SMAT-processed by high velocity steel balls (1 mm in diameter), and the impact velocity (80 ± 10 m/s) and the processing time (5–10 min) are varied to produced several different as-SMATed samples. More information on SMAT can be found elsewhere [31]. After SMAT, the thickness of the specimens is reduced to about 1 mm. After SMAT, the specimens are annealed in a short time (at 900 °C for 5 min) and aged at 700 °C for 1 h. The samples after short-time annealing and aging are referred as the SMAT-Aged samples here.

The quasi-static tensile tests and load-unload-reload (LUR) tests were conducted at room temperature and at a strain rate of 5×10^{-4} /s using displacement control. The specimens were cut from the SMATed disks and have dimensions of 10 × 2.5 × 1 mm^3 (according to the ISO6892-1998 standard). An extensometer was utilized to accurately measure and control the displacement during both tensile and LUR tests. The other details for LUR tests can be found in our previous research [28,32]. The distributions of microhardness along the depth for the gradient samples prior to and after tensile tests were obtained using a Vickers diamond indenter under a load of 25 g for 15 s dwell time. For each point, five groups of indentations were conducted, the average hardness value was taken and the error bar was provided. Prior to and after tensile tests, electron back-scattered diffraction (EBSD), transmission electron microscopy (TEM) and high-resolution TEM (HRTEM) were utilized to characterize the microstructures. The sample preparation and the other details for EBSD, TEM and HREM can be found elsewhere [13].

3. Results and discussions

3.1. Microstructure characterization prior to tensile testing

The microstructures along the depth for one typical as-SMATed sample and the corresponding SMAT-Aged sample are characterized and revealed in Figs. 1 and 2, respectively. The relative volume fractions of $L1_2$ phase in the FCC matrix at the topmost layer and at the core for these two samples are also estimated by XRD spectra, as shown in Fig. 3. $L1_2$ precipitates are coherent with the FCC matrix, thus the (311) fundamental overlap peaks are used to differentiate the contributions of the FCC and $L1_2$ phases by Gauss function fitting (as indicated in the Fig. 3b). In Figs. 1 and 2, the map of kernel average misorientation (KAM) values, the distributions of low-angle and high-angle GBs, the inverse pole figure (IPF) and phase maps, are given. The density of GNDs can generally be reflected by the KAM value [28,32].

For the as-SMATed sample, the KAM values and the density of low-angle GBs show a similar gradient distribution along the depth, indicating the gradient structure for substructures (dislocation walls and cells). Moreover, the densities of high-angle GBs are also observed to display a gradient along the depth, indicating a grain size gradient along the depth. The distributions of the volume fraction of B2 phase along the depth were measured based on the EBSD phase maps. First, we divided the phase map into fine bins only along the depth direction, and each bin had a height of 25 μm and a width of 200 μm. Then, the average volume fraction of B2 phase was calculated in each bin with a certain depth. The volume fraction of B2 phase for each certain depth is plotted along the depth, and the B2 phase is found to be homogeneously distributed along the depth (Fig. 1f). Moreover, the relative volume fractions of $L1_2$ phase in the FCC matrix for the topmost layer and for the core layers in the as-SMATed sample are estimated to be about 27% and 25 %, respectively, which indicates that the distribution of $L1_2$ phase along the depth is also relatively homogeneous. Thus, the as-SMATed sample can be considered as a gradient structure only for defects (GBs, including high-angle and low-angle GBs), resulting in a hardness gradient along the depth for the as-SMATed sample (Fig. 1g). It should be noted that the hardness of the core layer is higher than the un-SMATed CG sample,

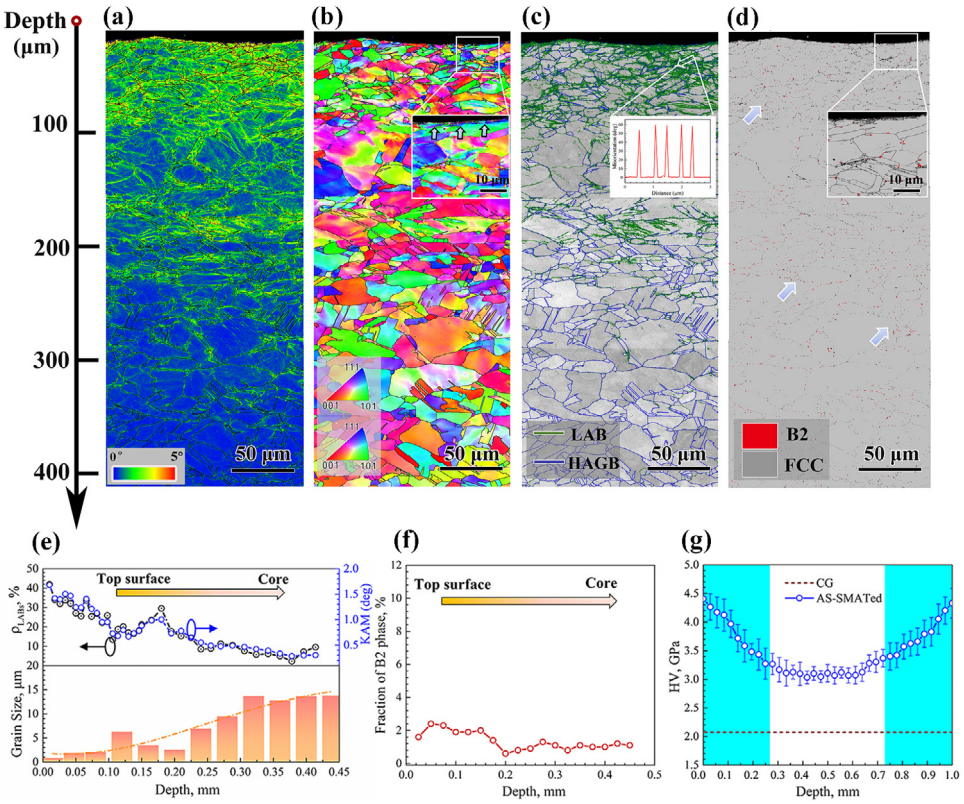

Fig. 1. Typical gradient microstructure for the as-SMATed sample. (a) The KAM map along the depth. (b) The IPF map along the depth. (c) The image with low-angle and high-angle GBs. (d) The phase map along the depth. (e) The distributions for density of low-angle GBs, KAM value and grain size along the depth. (f) The volume fraction of B2 phase with respect to the depth. (g) The microhardness distribution along the depth.

indicating that the influenced region by SMAT is across the whole sample.

For the SMAT-Aged sample (Fig. 2), the distributions of KAM values and the density of low-angle GBs show a peak at the depth of about 100 μm, while the grain size shows a similar gradient along the depth. Moreover, the volume fraction of B2 phase also displays a decreasing gradient from the surface to the core. Based on XRD spectra (Fig. 3a and b), the relative volume fraction of $L1_2$ phase in the FCC matrix for the topmost layer (69%) is observed to be much higher than that for the core layer (34%) in the SMAT-aged sample. Thus, the volume fraction of $L1_2$ phase also shows a gradient along the depth for the SMAT-Aged sample, besides the gradient distribution for the B2 phase. The formation of phase volume fractions (B2 and $L1_2$ phases) along the depth should be due to the graded magnitude for plastic deformation during SMAT and the subsequent aging. The stored plastic deformation energy should show a gradient distribution along the depth after SMAT, thus the topmost layer with highest energy state and highest defects (short-circuit diffusion) should have the greatest potential for formation of B2 and $L1_2$ phases during the subsequent aging, resulting in phase gradients along the depth.

In order to characterize the detailed microstructures, TEM observations at the topmost layer (within 100 μm from the surface) and at the core for the SMAT-aged sample are presented in Fig. 3c–f. Both the FCC phase and the $L1_2$ phase can be identified by selected area diffraction (SAD) patterns in the insets of Fig. 3c and d. The dislocation structure at the topmost layer is shown in Fig. 3b, numerous equiaxed dislocation cells and cell walls (with size of several hundred of nm) are observed, corresponding to the observed massive low-angle GBs in Fig. 2c. Every cell wall has a thickness of several tens of nm, and is decorated with a high density of dislocations. As a contrast, no dislocation cells and cell walls are observed at the core, only some isolated dislocations can be observed in the grain interior and the dislocation density is much lower at the core (Fig. 3d). Dark-field TEM images for characterizing the size, the morphology and the relative volume fraction of $L1_2$ phase in the FCC matrix for the topmost layer and the core layer are displayed in Fig. 3e and f, in which the brighter particles represent $L1_2$ phase. The average sizes of $L1_2$ particles at the topmost and the core layers are both estimated to be about 7 nm, and the relative volume fractions of $L1_2$ phase in the FCC matrix obtained from these dark-field TEM images are in consistent with the XRD results. Thus, the hardness gradient (as indicated in Fig. 2g) is induced by a heterogeneous structure with combined gradients (density of GBs, phase volume fractions for both B2 and $L1_2$ phases) along the depth.

The EDS mappings for an area with a B2 particle are displayed in Fig. 4a, while the element distributions along the marked line in Fig. 4a are displayed in Fig. 4b. As indicated, both Al and Ni elements are enriched in the B2 particle [45]. The EDS mappings for the FCC matrix with $L1_2$ nano-precipitates are shown in Fig. 4c, while the element distributions along the marked line in Fig. 4c are displayed in Fig. 4d. It is shown that Ni element is highly enriched (about 63%) and Al element is slightly enriched in the $L1_2$ phase in this HEA [45]. In general, Al atoms most likely occupy the corner position while Ni atoms most likely occupy the face center position for the $L1_2$ phase [45]. Generally, Al atoms most likely occupy the corner position while Ni atoms most likely occupy the body center position for the B2 phase [47]. The coherent $L1_2$ nanoprecipitates should be significantly beneficial to both strength and ductility, the B2 nanoprecipitates should have strong positive influence on the strength while have less influence on the ductility.

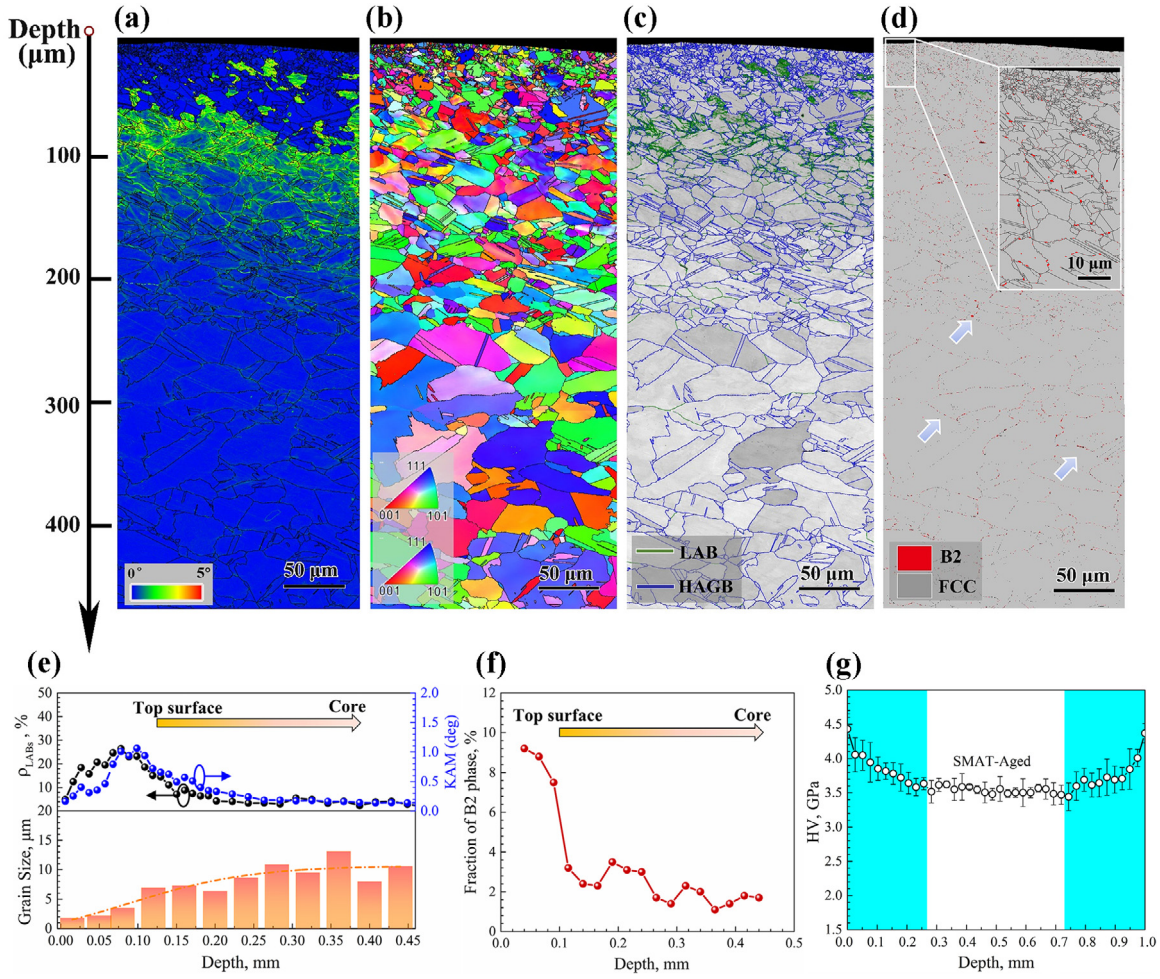

Fig. 2. Microstructure with combined gradients for the SMAT-Aged sample. (a) The KAM map along the depth. (b) The IPF map along the depth. (c) The image with low-angle and high-angle GBs. (d) The phase map along the depth. (e) The distributions for density of low-angle GBs, KAM value and grain size along the depth. (f) The volume fraction of B2 phase as a function of depth. (g) The microhardness distribution along the depth.

3.2. Tensile properties, hardness distributions after deformation and HDI hardening

In order to illustrate the effects of the defect gradient (as-SMATed samples) and the combined gradients (SMAT-Aged samples) on the tensile properties (as compared to the as-annealed sample), a series of tensile tests have been conducted and the corresponding engineering stress-strain curves on the typical samples are displayed in Fig. 5a. The strain hardening rate Θ and the true stress are plotted as a function of true strain for these samples in Fig. 5b. After SMAT, the yield strength is elevated to about 890 MPa as compared to about 340 MPa for the as-annealed sample, while the uniform elongation is reduced to about 10 % from about 43 % for the as-annealed samples. Although the as-SMATed sample shows a good synergy of strength and ductility, the high yield strength is still obtained at the expense of the ductility. Remarkably, the SMAT-Aged sample shows a simultaneously improvement on the strength (about 960 MPa) and ductility (about 16%), as compared to the as-SMATed sample (about 890 MPa, 10%). Moreover, the strain hardening ability is also observed to be much higher in the SMAT-Aged sample compared to the as-SMATed sample. A transient up-turn phenomenon for hardening rate is also observed for the SMAT-Aged sample. Moreover, the yield strength is plotted as a function of uniform elongation for all as-SMATed samples and the corresponding SMAT-Aged samples in Fig. 5c. It is shown that the SMAT-Aged samples with combined gradients always have a better synergy of strength and ductility over the as-SMATed samples with a single gradient, and the corresponding deformation and microstructural mechanisms would be revealed next.

The strong strain hardening behavior for the SMAT-Aged sample raises a critical question: How does each layer contribute to the overall strain hardening? To resolve this issue, the microhardness distributions and the distributions of hardness increments ($\triangle H$) after tensile deformation for the as-annealed sample, the as-SMATed and the SMAT-Aged samples are obtained and displayed in Fig. 6a and b, respectively. $\triangle H$ can generally be considered as an indicator on the magnitude of retained hardening after tensile deformation. For the as-SMATed sample, the topmost layer shows nearly no strain hardening and the strain hardening behavior of the whole sample is mostly accommodated by the core. However, each layer in the SMAT-Aged sample makes a contribution to the strain hardening. It is amazingly observed that the strain hardening ability for most part of the SMAT-Aged sample is even higher than that of the as-annealed sample with CGs.

In the heterogeneous structures, such as gradient structures and heterogeneous grain structures [28,29,31–33], back stress can be induced among different layers at various depths or grains with different sizes due to the plastic deformation incompatibility between theses hard and soft domains, resulting in strong HDI hardening. In the SMAT-Aged samples with structures with combined gradients, various layers at different depths can be considered as larger hard/soft domains, while different phases at each layer can

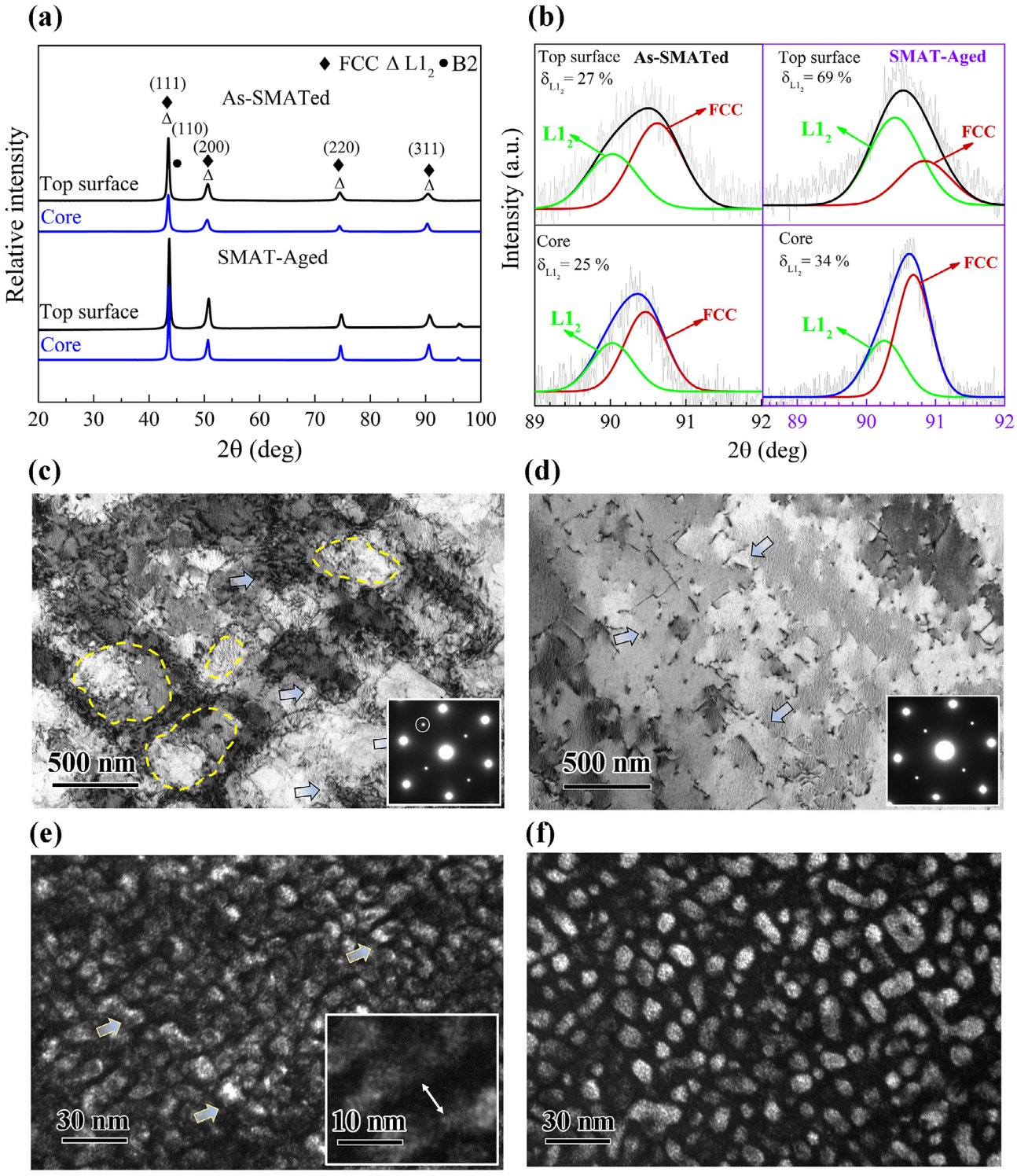

Fig. 3. (a) The XRD spectra at the topmost and central layers for the typical As-SMATed and SMAT-Aged samples. (b) The overlapped (311) asymmetric peaks and the corresponding Gauss function fittings of FCC phase and $L1_2$ phase. Bright-field (c,d) and dark-field TEM (e,f) images for characterizing the size and the relative volume fraction of $L1_2$ phase in the FCC matrix for the SMAT-Aged sample: (c,e) at the topmost layer; (d,f) at the core layer.

be considered as smaller hard/soft domains. Thus, the HDI hardening should plan a more important role in such a dual heterogeneous structure. Thus, LUR tests were conducted on the as-SMATed and the SMAT-Aged samples to reveal and compared the effect of the structures with combined gradients on the HDI hardening. The true stress-strain curves of LUR tests for these two samples are shown in Fig. 7a. The HDI stress (σ_{HDI}) and the HDI hardening rate are plotted as a function of true strain for these two samples in Fig. 7b. The back stress (HDI stress) were calculated based on the method proposed in our previous paper [28]. As indicated in Fig. 7b, the SMAT-Aged sample show a higher HDI stress and a higher HDI hardening rate than the as-SMATed sample. These observations confirm that the HDI hardening has a higher influence on the structures with combined gradients than the struc-

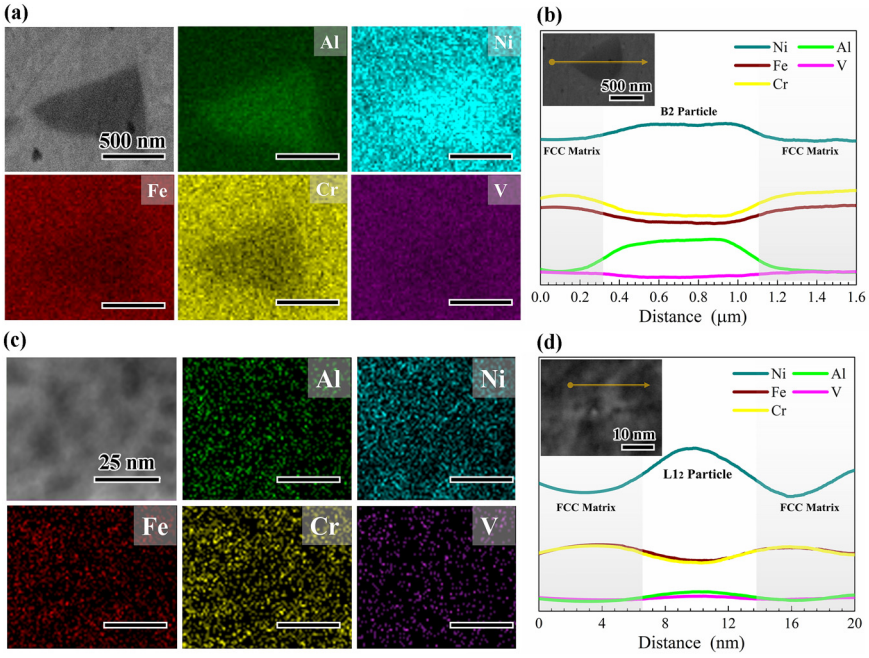

Fig. 4. (a) EDS mappings for an area with a B2 particle. (b) The element distributions along the marked line in (a). (c) EDS mappings for the FCC matrix with $L1_2$ nano-precipitates. (d) The element distributions along the marked line in the inset.

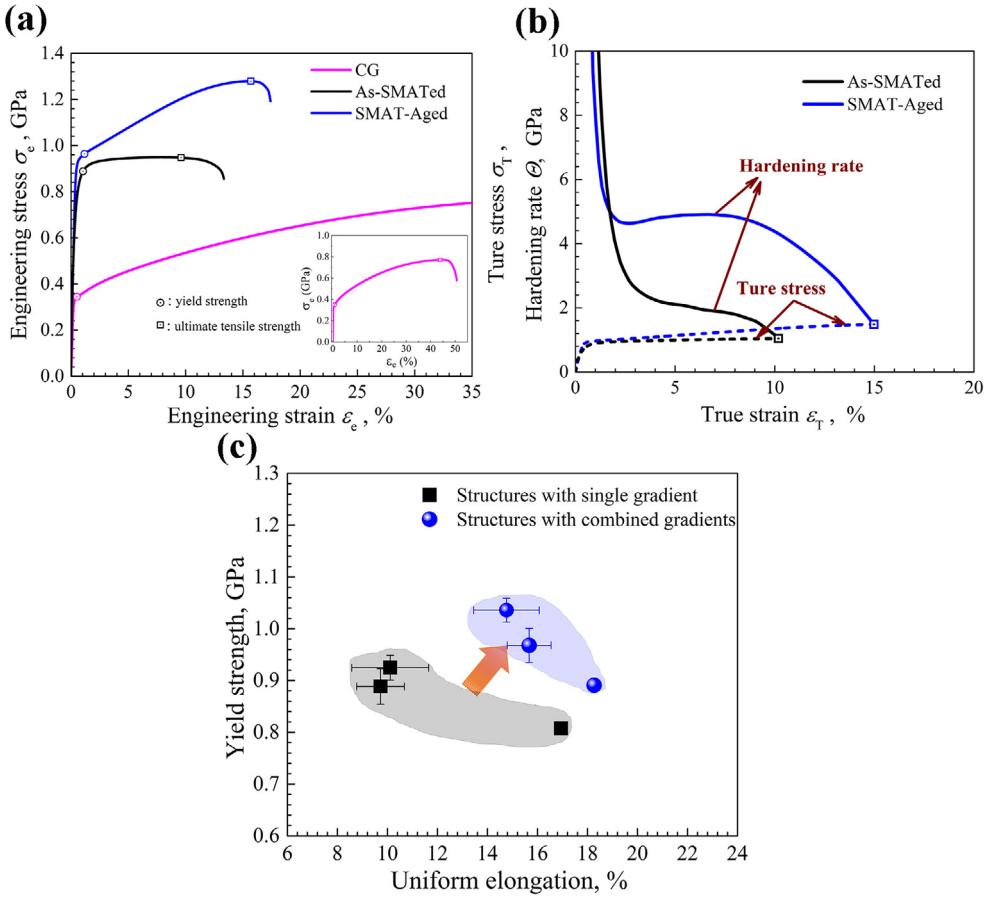

Fig. 5. Tensile properties for various samples. (a) Engineering stress-strain curves. (b) Hardening rate and true stress as a function of true strain. (c) Yield strength as a function of uniform elongation for all tested samples in the present study.

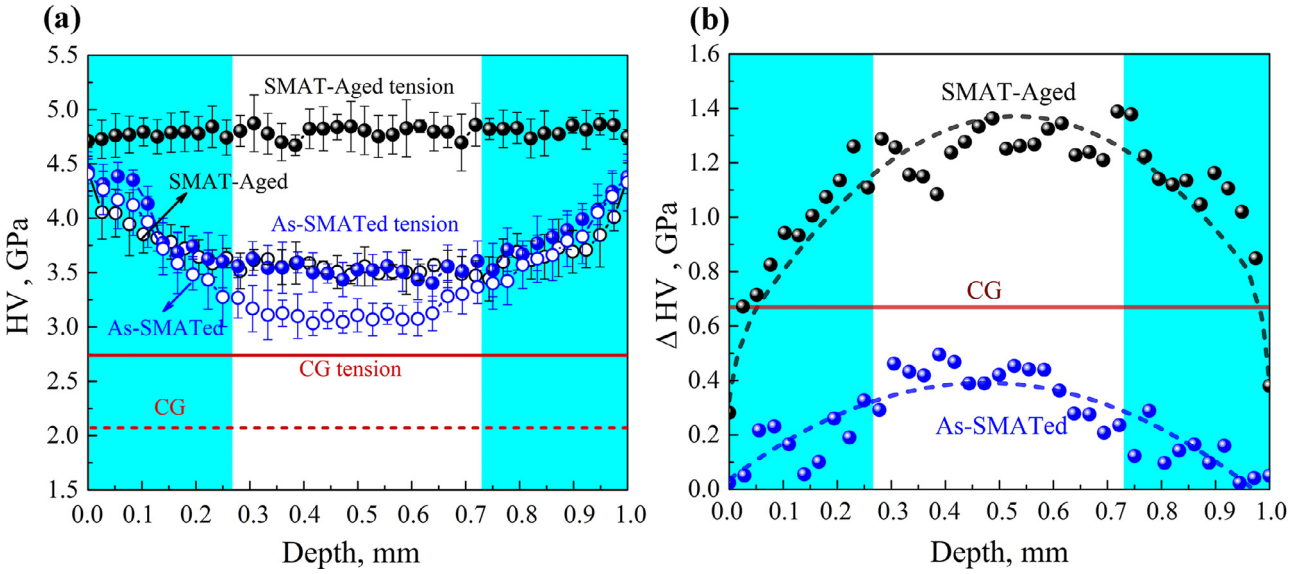

Fig. 6. (a) The microhardness distributions along the depth prior to and after tensile deformation for the as-annealed sample, the as-SMATed and the SMAT-Aged samples. (b) The distributions of hardness increments after tensile deformation for all three samples.

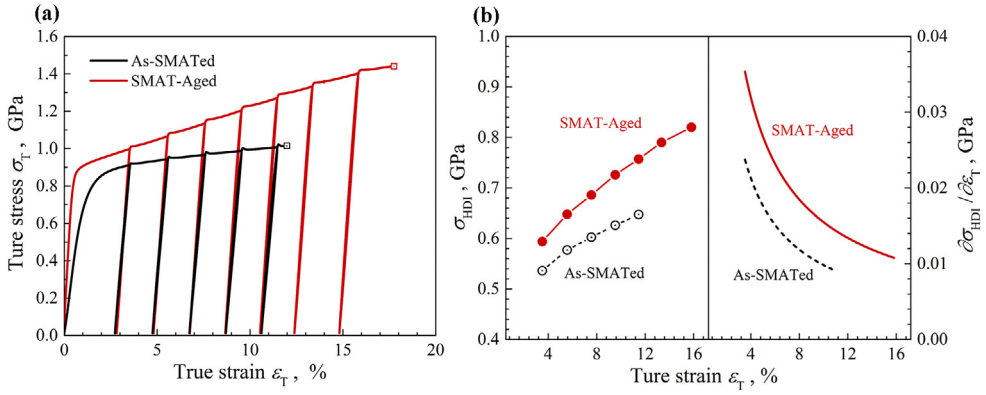

Fig. 7. HDI hardening for the as-SMATed and the SMAT-Aged samples. (a) True stress-strain curves for LUR tests. (b) σ_{HDI} and HDI hardening rate as a function of true strain.

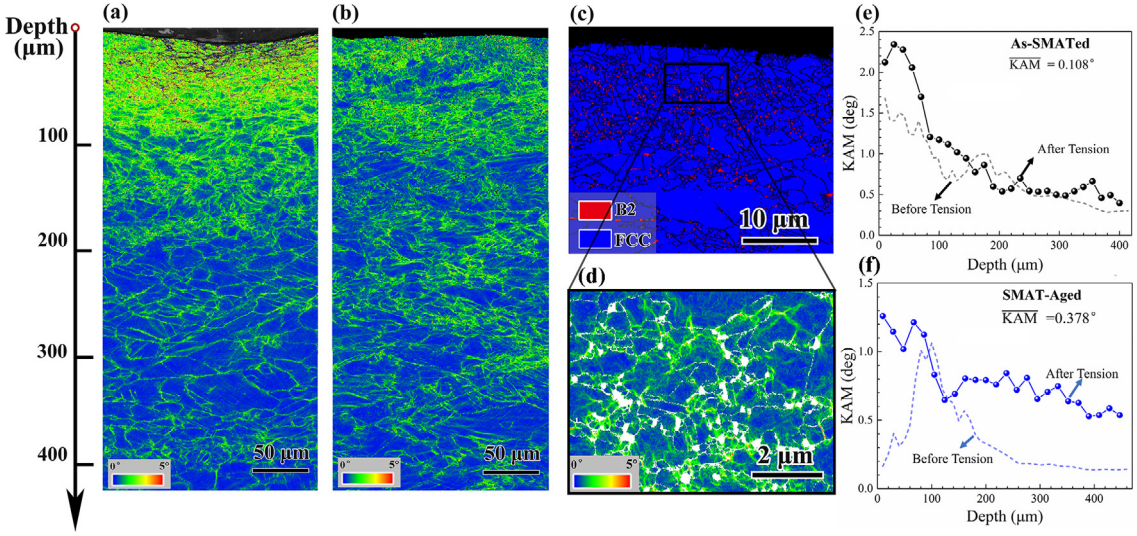

Fig. 8. KAM mappings for (a) the as-SMATed sample; (b) the SMAT-Aged sample. Close-up views of (c) phase mapping and (d) KAM mapping for the topmost layer of the SMAT-Aged sample. The distributions of the average KAM value along the depth prior to and after tensile testing for (e) the as-SMATed sample; (f) the SMAT-Aged sample.

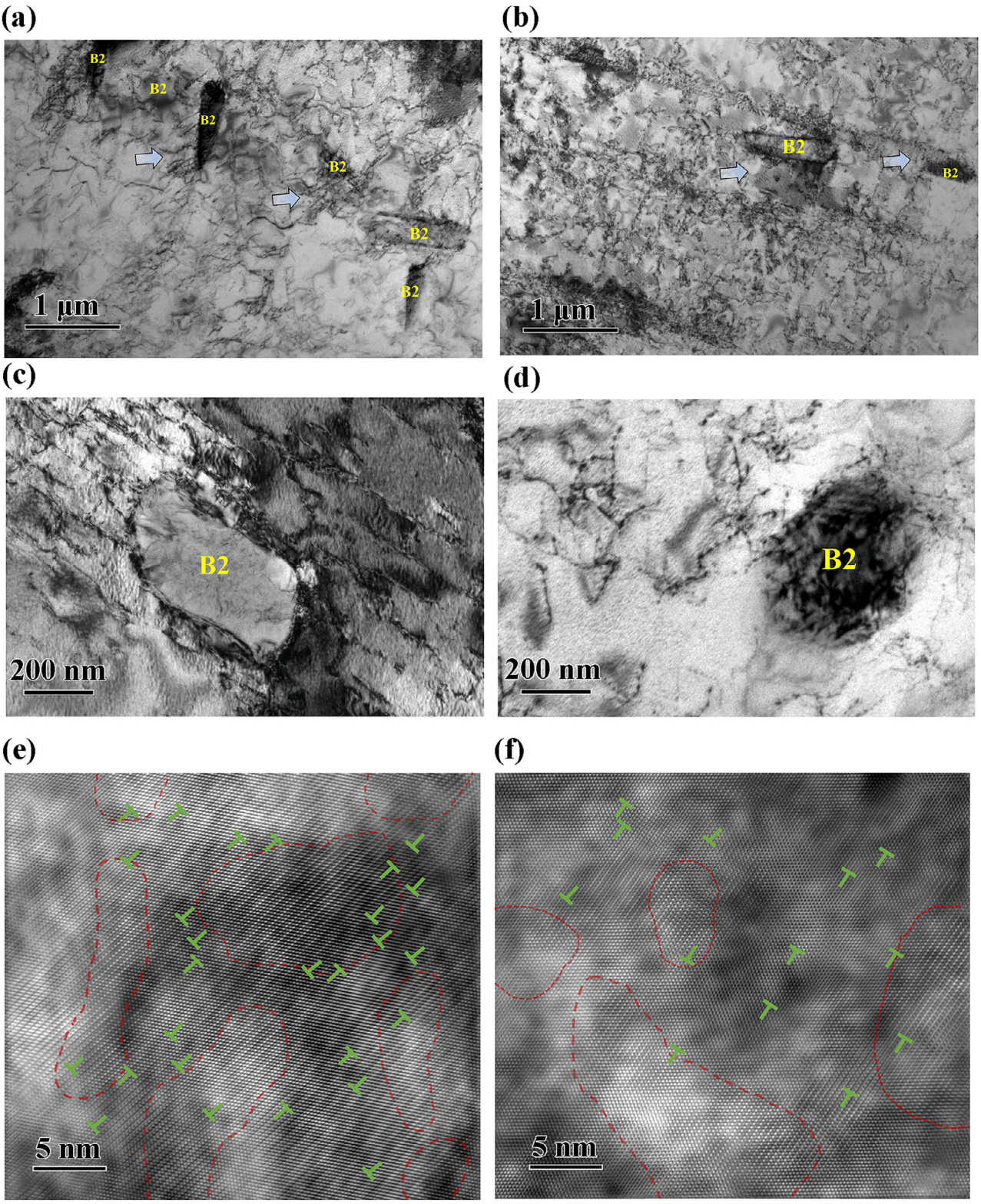

Fig. 9. TEM and HRTEM observations after tensile testing for the SMAT-Aged sample. Bright-field TEM images (a, c) for the topmost layer; (b, d) for the central layer. HRTEM images showing interaction and accumulation of dislocations with $L1_2$ nano-particles in the SMAT-Aged sample (e) for the topmost layer; (f) for the central layer. (e) and (f) are obtained after fast Fourier transformation (FFT) and inverse FFT, and $L1_2$ nano precipitates are also circled by red lines in these two images. (For interpretation of the references to color in this figure legend, the reader is referred to the web version of this article).

tures with single gradient, resulting in a better tensile property in structures with combined gradients.

3.3. The deformation and microstructural mechanisms during tensile loading

In the structures with combined gradients, GNDs can be produced at the boundaries of each layer or at various phase boundaries, and these GNDs generated between hard and soft domains can result in strong HDI hardening for excellent tensile properties [31–33]. In this regard, the KAM mappings after tensile deformation for the as-SMATed sample and the SMAT-Aged sample are shown in Fig. 8a and b, respectively. The close-up views of phase and KAM value mappings for the topmost layer of the SMAT-Aged sample is shown in Fig. 8c and d. In Fig. 8d, B2 phase is highlighted by white color. It is interesting to note that much higher KAM value is observed at the adjacent area of phase boundaries of B2 and FCC matrix. The KAM value is averaged at each depth, then the distributions of the average KAM value along the depth prior to and after tensile testing are displayed for the as-SMATed sample and the SMAT-Aged sample in Fig. 8e and f, respectively. The increment of the average KAM value after tensile deformation for the whole as-SMATed sample is estimated to be about 0.108^0, which is much smaller than that for the SMAT-Aged sample (0.378^0). These observations indicate that the structures with combined gradients can induce more severe strain gradients and produce higher increment for GND density at various domain boundaries, resulting in stronger HDI hardening for better tensile properties.

TEM and HRTEM images after tensile deformation for the topmost layer and the central layer in the SMAT-Aged sample are shown in Fig. 9. Higher volume fraction of B2 phase is observed at the topmost layer, as compared to the central layer. Massive dislocations are observed to be accumulated around the B2 particles. Dislocation pile-ups against B2 particles can also be clearly observed. High density of bowing full dislocations are observed to be blocked and ends of bowing dislocations are pinned by B2 particles. Higher externally stress should be applied to bow-out B2 particles due to the observed bulging dislocation lines around B2 nano-particles. Thus, B2 particles with hundreds of nm at size and interspacing should be effective on the bowing (by-pass) strengthening/hardening.

It is indicated earlier that the relative volume fraction of $L1_2$ phase also has a gradient along the depth, and the topmost layer has the highest volume fraction of $L1_2$ phase. HRTEM observations after tensile deformation (based on numerous HRTEM images) confirm this. Moreover, the interaction mechanisms between dislocations and $L1_2$ nanoprecipitates can be identified by these HRTEM images (Fig. 9e and f). It should be interestingly noted that dislocations are mostly accumulated either near or inside $L1_2$ nanoprecipitates, resulting in higher density of dislocations at these areas. It is also observed that higher density of dislocations can be accumulated around $L1_2$ nanoprecipitates at the topmost layer (Fig. 9e) as compared to the center layer (Fig. 9f). We can rationalize that the $L1_2$ nanoprecipitates are deformable due to the observed numerous dislocations in the interior of $L1_2$ nanoprecipitates and the elongated shape, thus the shearing mechanism should be primarily responsible for the strengthening/hardening of $L1_2$ phase. The size and interspacing of $L1_2$ nanoprecipitates at the central layer are several nm and tens of nm, and the interspacing is even smaller at the topmost layer, which should be very effective on accumulating dislocations around $L1_2$ nanoprecipitates and on the shearing strengthening/hardening, resulting in better synergy of strength and ductility in the structures with combined gradients than in the structures with single gradient. The topmost layer has the highest volume fractions of B2 and $L1_2$ phases, thus B2 and $L1_2$ nanoprecipitates should provide the strongest precipitation strengthening at the topmost layer, which compensates the diminished strain hardening due to the reduced grain size at the topmost layer and results in better tensile ductility in the structures with combined gradients.

3.4. Discussions on the strengthening and strain hardening of structures with combined gradients

Generally, the followed aspects should be considered for the yield strength of metals and alloys: the solid-solution strengthening part (σ_{ss}), the dislocation strengthening part (σ_{dis}), the grain-boundary strengthening part (σ_{gb}), the precipitation strengthening part (σ_{ps}) and the HDI strengthening part (σ_{HDI}). As indicated in the microstructure characterizations prior to tensile testing (Figs. 1–3), the solid-solution strengthening and the grain-boundary strengthening should have similar contributions to the structures with combined gradients and the structures with single gradient. Although the structures with combined gradients have less contribution from dislocation strengthening than the structures with single gradient (as indicated by the lower average KAM value in Fig. 8 for the structures with combined gradients prior to tensile testing), the precipitation strengthening and the HDI strengthening should play much more important role in the structures with combined gradients, resulting in higher yield strength. In the precipitation-hardened alloys, the strengthening by the by-passing precipitates and the shearing precipitates is highly dependent on the volume fraction and the interspacing of precipitates. The volume fractions of both B2 and $L1_2$ phases are much higher, and the interspacings of these two kinds of precipitates are much smaller in the structures with combined gradients, resulting in higher contribution of precipitation strengthening in the structures with combined gradients. Moreover, the structures with combined gradients have a more severe heterogeneity, thus has higher HDI strengthening contribution than the structures with single gradient [33,35]. Thus, the observed higher yield strength in the structures with combined gradients can be attributed to the higher contributions from both precipitation strengthening and HDI strengthening.

The better uniform elongation in the structures with combined gradients can be due to the following three aspects: (i) the lower retained dislocation density after short-time annealing and aging; (ii) the higher bowing (by-pass) hardening for B2 nanoprecipitates and the shearing hardening for $L1_2$ nanoprecipitates; (iii) and the higher HDI hardening. The dismantlement of original dislocation substructure by annealing and aging will leave more room in the grain interiors of the structures with combined gradients for the formation of new dislocations and dislocation networks. Moreover, stronger HDI hardening and precipitation hardening should also help on accumulating dislocations in the grain interiors of the structures with combined gradients for better tensile ductility.

4. Summary and concluding remarks

In the present study, the structures with single gradient and combined gradients have been architected and fabricated in a $Al_{0.5}Cr_{0.9}FeNi_{2.5}V_{0.2}$ HEA utilizing SMAT and heat-treatment. Then, the tensile properties and the corresponding deformation mechanisms have been investigated and revealed, and the findings are summarized as follows:

(1) Both grain size (high-angle and low angle GBs) and volume fraction of precipitates ($L1_2$ and B2) are observed to show gradient distributions along the depth after short-time annealing and aging, forming structures with combined gradients with a more severe heterogeneity. The structures with combined gradients are observed to have both higher yield strength and larger uniform elongation, as compared to the corresponding structures with single gradient.

(2) The topmost layer of the structure with single gradient shows nearly no strain hardening, while each layer in the structure with combined gradients has a contribution to the overall strain hardening and the strain hardening ability for most part of the structure with combined gradients is even higher than that of the homogeneous structure with CGs. More severe strain gradient and higher density of GNDs are found to be induced at various domain boundaries in the structures with combined gradients, resulting in stronger HDI strengthening/hardening for better tensile properties.
(3) Bowing hardening and shearing hardening mechanisms are observed for $L1_2$ and B2 precipitates, respectively. The interspacing of $L1_2$ and B2 nanoprecipitates are at tens or hundreds of nm, which should be very effective on the precipitation strengthening/hardening by accumulating dislocations at phase interfaces.
(4) The observed higher yield strength in the structures with combined gradients can be attributed to the higher contributions from both precipitation strengthening and HDI strengthening, which overwhelm the less contribution from dislocation strengthening. The better uniform elongation in the structures with combined gradients can be due to the lower retained dislocation density after heat-treatment, higher HDI hardening and precipitation hardening. The present results should provide insights for achieving extraordinary tensile properties in HEAs by deploying structures with combined gradients.

Declaration of Competing Interest

The authors declare that they have no known competing financial interests or personal relationships that could have appeared to influence the work reported in this paper.

Acknowledgements

This research was supported by the National Key R&D Program of China [grant number 2017YFA0204402]; the NSFC Basic Science Center Program for "Multiscale Problems in Nonlinear Mechanics" [grant number 11988102], the National Natural Science Foundation of China [grant numbers 11790293, 52192591], the fellowship of China Postdoctoral Science Foundation [grant number 2021M703292], and the Strategic Priority Research Program of the Chinese Academy of Sciences [grant number XDB22040503].

References

[1] J.W. Yeh, S.K. Chen, S.J. Lin, J.Y. Gan, T.S. Chin, T.T. Shun, C.H. Tsau, S.Y. Chang, Nanostructured high-entropy alloys with multiple principal elements: novel alloy design concepts and outcomes, Adv. Eng. Mater. 6 (2004) 299–303.
[2] B. Gludovatz, A. Hohenwarter, D. Catoor, E.H. Chang, E.P. George, R.O. Ritchie, A fracture-resistant high-entropy alloy for cryogenic applications, Science 345 (2014) 1153–1158.
[3] B. Schuh, F. Mendez-Martin, B. Völker, E.P. George, H. Clemens, R. Pippan, A. Hohenwarter, Mechanical properties, microstructure and thermal stability of a nanocrystalline CoCrFeMnNi high-entropy alloy after severe plastic deformation, Acta Mater. 96 (2015) 258–268.
[4] Z.M. Li, K.G. Pradeep, Y. Deng, D. Raabe, C.C. Tasan, Metastable high-entropy dual-phase alloys overcome the strength–ductility trade-off, Nature 534 (2016) 227–230.
[5] Z.F. Lei, X.J. Liu, Y. Wu, H. Wang, S.H. Jiang, S.D. Wang, X.D. Hui, Y.D. Wu, B. Gault, P. Kontis, D. Raabe, L. Gu, Q.H. Zhang, H. Chen, H.T. Wang, J.B. Liu, K. An, Q.S. Zeng, T.G. Nieh, Z.P. Lu, Enhanced strength and ductility in a high-entropy alloy via ordered oxygen complexes, Nature 563 (2018) 546–550.
[6] E.P. George, D. Raabe, R.O. Ritchie, High-entropy alloys, Nat. Rev. Mater. 4 (2019) 515–534.
[7] Z.L. Yang, M.X. Yang, Y. Ma, L.L. Zhou, W.Q. Cheng, F.P. Yuan, X.L. Wu, Strain rate dependent shear localization and deformation mechanisms in the CrMnFeCoNi high-entropy alloy with various microstructures, Mater. Sci. Eng. A 793 (2020) 139854.
[8] P. Shi, R. Li, Y. Li, Y. Wen, Y. Zhong, W. Ren, Z. Shen, T. Zheng, J. Peng, X. Liang, P. Hu, N. Min, Y. Zhang, Y. Ren, P.K. Liaw, D. Raabe, Y.D. Wang, Hierarchical crack buffering triples ductility in eutectic herringbone high-entropy alloys, Science 373 (2021) 912–918.
[9] B. Gludovatz, A. Hohenwarter, K.V.S. Thurston, H.B. Bei, Z.G. Wu, E.P. George, R.O. Ritchie, Exceptional damage-tolerance of a medium-entropy alloy CrCoNi at cryogenic temperatures, Nat. Commun. 7 (2016) 10602.
[10] J. Miao, C.E. Slone, T.M. Smith, C. Niu, H. Bei, M. Ghazisaeidi, G.M. Pharr, M.J. Mills, The evolution of the deformation substructure in a Ni-Co-Cr equiatomic solid solution alloy, Acta Mater. 132 (2017) 35–48.
[11] Y. Ma, F.P. Yuan, M.X. Yang, P. Jiang, E. Ma, X.L. Wu, Dynamic shear deformation of a CrCoNi medium-entropy alloy with heterogeneous grain structures, Acta Mater. 148 (2018) 407–418.
[12] M.X. Yang, L.L. Zhou, C. Wang, P. Jiang, F.P. Yuan, E. Ma, X.L. Wu, High impact toughness of CrCoNi medium-entropy alloy at liquid-helium temperature, Scr. Mater. 172 (2019) 66–71.
[13] X.L. Wu, M.X. Yang, P. Jiang, C. Wang, L.L. Zhou, F.P. Yuan, E. Ma, Deformation nanotwins suppress shear banding during impact test of CrCoNi medium-entropy alloy, Scr. Mater. 178 (2020) 452–456.
[14] C.E. Slone, J. Miao, E.P. George, M.J. Mills, Achieving ultra-high strength and ductility in equiatomic CrCoNi with partially recrystallized microstructures, Acta Mater. 165 (2019) 496–507.
[15] J. Ding, Q. Yu, M. Asta, R.O. Ritchie, Tunable stacking fault energies by tailoring local chemical order in CrCoNi medium-entropy alloys, Proc. Natl. Acad. Sci. U. S. A. 115 (2018) 8919–8924.
[16] Y. Ma, M.X. Yang, F.P. Yuan, X.L. Wu, Deformation induced hcp nano-lamella and its size effect on the strengthening in a CoCrNi medium-entropy alloy, J. Mater. Sci. Technol. 82 (2021) 122–134.
[17] M.X. Yang, D.S. Yan, F.P. Yuan, P. Jiang, E. Ma, X.L. Wu, Dynamically reinforced heterogeneous grain structure prolongs ductility in a medium-entropy alloy with gigapascal yield strength, Proc. Natl. Acad. Sci. 115 (2018) 7224–7229.
[18] Q.J. Li, H. Sheng, E. Ma, Strengthening in multi-principal element alloys with local-chemical-order roughened dislocation pathways, Nat. Commun. 10 (2019) 3563.
[19] R.P. Zhang, S.T. Zhao, J. Ding, Y. Chong, T. Jia, C. Ophus, M. Asta, R.O. Ritchie, A.M. Minor, Short-range order and its impact on the CrCoNi medium-entropy alloy, Nature 581 (2020) 283–287.
[20] A. Fantin, G.O. Lepore, A.M. Manzoni, S. Kasatikov, T. Scherb, T. Huthwelker, F. d'Acapito, G. Schumacher, Short-range chemical order and local lattice distortion in a compositionally complex alloy, Acta Mater. 193 (2020) 329–337.
[21] W.R. Jian, Z.C. Xie, S.Z. Xu, Y.Q. Su, X.H. Yao, I.J. Beyerlein, Effects of lattice distortion and chemical short-range order on the mechanisms of deformation in medium entropy alloy CoCrNi, Acta Mater. 199 (2020) 352–369.
[22] Q.Q. Ding, Y. Zhang, X. Chen, X.Q. Fu, D. Chen, S.J. Chen, L. Gu, F. Wei, H.B. Bei, Y.F. Gao, M.R. Wen, J.X. Li, Z. Zhang, T. Zhu, R.O. Ritchie, Q. Yu, Tuning element distribution, structure and properties by composition in high-entropy alloys, Nature 574 (2019) 223–227.
[23] X.F. Chen, Q. Wang, Z.Y. Cheng, M. Zhu, H. Zhou, P. Jiang, L.L. Zhou, Q.Q. Xue, F.P. Yuan, J. Zhu, X.L. Wu, E. Ma, Direct observation of chemical short-range order in a medium-entropy alloy, Nature 592 (2021) 712–716.
[24] R.Z. Valiev, I.V. Alexandrov, Y.T. Zhu, T.C. Lowe, Paradox of strength and ductility in metals processed bysevere plastic deformation, J. Mater. Res. 17 (2002) 5–8.
[25] M.A. Meyers, A. Mishra, D.J. Benson, Mechanical properties of nanocrystalline materials, Prog. Mater. Sci. 51 (2006) 427–556.
[26] Z. Cheng, H. Zhou, Q. Lu, H. Gao, L. Lu, Extra strengthening and work hardening in gradient nanotwinned metals, Science 362 (2018) eaau1925.
[27] Q. Pan, L. Zhang, R. Feng, Q. Lu, K. An, A.C. Chuang, J.D. Poplawsky, P.K. Liaw, L. Lu, Gradient cell–structured high-entropy alloy with exceptional strength and ductility, Science 374 (2021) 984–989.
[28] M.X. Yang, Y. Pan, F.P. Yuan, Y.T. Zhu, X.L. Wu, Back stress strengthening and strain hardening in gradient structure, Mater. Res. Lett. 4 (2016) 145–151.
[29] T.H. Fang, W.L. Li, N.R. Tao, K. Lu, Revealing extraordinary intrinsic tensile plasticity in gradient nano-grained copper, Science 331 (2011) 1587–1590.
[30] Z. Zeng, X. Li, D. Xu, L. Lu, H. Gao, T. Zhu, Gradient plasticity in gradient nano–grained metals, Extreme Mech. Lett. 8 (2016) 213–219.
[31] X.L. Wu, P. Jiang, L. Chen, F.P. Yuan, Y.T. Zhu, Extraordinary strain hardening by gradient structure, Proc. Natl. Acad. Sci. 111 (2014) 7197–7201.
[32] X.L. Wu, M.X. Yang, F.P. Yuan, G.L. Wu, Y.J. Wei, X.W. Huang, Y.T. Zhu, Heterogeneous lamella structure unites ultrafine-grain strength with coarse-grain ductility, Proc. Natl. Acad. Sci. U. S. A. 112 (2015) 14501–14505.
[33] Y.T. Zhu, X.L. Wu, Perspective on hetero-deformation induced (HDI) hardening and back stress, Mater. Res. Lett. 7 (2019) 393–398.
[34] P.V. Liddicoat, X.Z. Liao, Y.H. Zhao, Y.T. Zhu, M.Y. Murashkin, E.J. Lavernia, R.Z. Valiev, S.P. Ringer, Nanostructural hierarchy increases the strength of aluminium alloys, Nat. Commun. 1 (2010) 63.
[35] G. Liu, G.J. Zhang, F. Jiang, X.D. Ding, Y.J. Sun, J. Sun, E. Ma, Nanostructured high-strength molybdenum alloys with unprecedented tensile ductility, Nat. Mater. 12 (2013) 344–350.
[36] S.H. Kim, H. Kim, N.J. Kim, Brittle intermetallic compound makes ultrastrong low-density steel with large ductility, Nature 518 (2015) 77–79.
[37] Z.W. Wang, W.J. Lu, H. Zhao, C.H. Liebscher, J.Y. He, D. Ponge, D. Raabe, Z.M. Li, Ultrastrong lightweight compositionally complex steels via dual-nanoprecipitation, Sci. Adv. 6 (2020) eaba9543.
[38] Y. Yang, T.Y. Chen, L.Z. Tan, J.D. Poplawsky, K. An, Y.L. Wang, G.D. Samolyuk, K. Littrell, A.R. Lupini, A. Borisevich, E.P. George, Bifunctional nanoprecipitates strengthen and ductilize a medium-entropy alloy, Nature 595 (2021) 245–249.
[39] T. Yang, Y.L. Zhao, Y. Tong, Z.B. Jiao, J. Wei, J.X. Cai, X.D. Han, D. Chen, A. Hu, J.J. Kai, K. Lu, Y. Liu, C.T. Liu, Multicomponent intermetallic nanoparticles and superb mechanical behaviors of complex alloys, Science 362 (2018) 933–937.

[40] B. Gwalani, V. Soni, D. Choudhuri, M. Lee, J.Y. Hwang, S.J. Nam, H. Ryu, S.H. Hong, R. Banerjee, Stability of ordered $L1_2$ and B_2 precipitates in face centered cubic based high entropy alloys – $Al_{0.3}CoFeCrNi$ and $Al_{0.3}CuFeCrNi_2$, Scr. Mater. 123 (2016) 130–134.
[41] Y.Y. Zhao, H.W. Chen, Z.P. Lu, T.G. Nieh, Thermal stability and coarsening of coherent particles in a precipitation-hardened $(NiCoFeCr)_{94}Ti_2Al_4$ high-entropy alloy, Acta Mater. 147 (2018) 184–194.
[42] J.C. Rao, H.Y. Diao, V. Ocelík, D. Vainchtein, C. Zhang, C. Kuo, Z. Tang, W. Guo, J.D. Poplawsky, Y. Zhou, P.K. Liaw, J.Th.M. De Hosson, Secondary phases in AlxCoCrFeNi high-entropy alloys: An *in-situ* TEM heating study and thermodynamic appraisal, Acta Mater. 131 (2017) 206–220.
[43] X.H. Du, W.P. Li, H.T. Chang, T. Yang, G.S. Duan, B.L. Wu, J.C. Huang, F.R. Chen, C.T. Liu, W.S. Chuang, Y. Lu, M.L. Sui, E.W. Huang, Dual heterogeneous structures lead to ultrahigh strength and uniform ductility in a Co-Cr-Ni medium-entropy alloy, Nat. Commun. 11 (2020) 2390.
[44] Y. Tong, D. Chen, B. Han, J. Wang, R. Feng, T. Yang, C. Zhao, Y.L. Zhao, W. Guo, Y. Shimizu, C.T. Liu, P.K. Liaw, K. Inoue, Y. Nagai, A. Hu, J.J. Kai, Outstanding tensile properties of a precipitation-strengthened $FeCoNiCrTi_{0.2}$ high-entropy alloy at room and cryogenic temperatures, Acta Mater. 165 (2019) 228–240.
[45] Y.J. Liang, L.J. Wang, Y.R. Wen, B.Y. Cheng, Q.L. Wu, T.Q. Cao, Q. Xiao, Y.F. Xue, G. Sha, Y.D. Wang, Y. Ren, X.Y. Li, L. Wang, F.C. Wang, H.N. Cai, High-content ductile coherent nanoprecipitates achieve ultrastrong high-entropy alloys, Nat. Commun. 9 (2018) 4063.
[46] F. He, Z.S. Yang, S.F. Liu, D. Chen, W.T. Lin, T. Yang, D.X. Wei, Z.J. Wang, J.C. Wang, J.J. Kai, Strain partitioning enables excellent tensile ductility in precipitated heterogeneous high-entropy alloys with gigapascal yield strength, Int. J. Plast. 144 (2021) 103022.
[47] D. Farkas, B. Mutasa, C. Vailhe, K. Ternes, Interatomic potentials for B2 NiAl and martensitic phases, Model. Simul. Mater. Sci. Eng. 3 (1995) 201–214.